A Cloud Microphysics Parameterization for Shallow Cumulus Clouds Based on Lagrangian Cloud Model Simulations

YIGN NOH AND DONGGUN OH

Department of Atmospheric Sciences, Yonsei University, Seoul, South Korea

FABIAN HOFFMANN[a] AND SIEGFRIED RAASCH

Institute of Meteorology and Climatology, Leibniz Universität Hannover, Hannover, Germany

(Manuscript received 10 March 2018, in final form 2 August 2018)

ABSTRACT

Cloud microphysics parameterizations for shallow cumulus clouds are analyzed based on Lagrangian cloud model (LCM) data, focusing on autoconversion and accretion. The autoconversion and accretion rates, A and C, respectively, are calculated directly by capturing the moment of the conversion of individual Lagrangian droplets from cloud droplets to raindrops, and it results in the reproduction of the formulas of A and C for the first time. Comparison with various parameterizations reveals the closest agreement with Tripoli and Cotton, such as $A = \alpha N_c^{-1/3} q_c^{7/3} H(R - R_T)$ and $C = \beta q_c q_r$, where q_c and N_c are the mixing ratio and the number concentration of cloud droplets, q_r is the mixing ratio of raindrops, R_T is the threshold volume radius, and H is the Heaviside function. Furthermore, it is found that α increases linearly with the dissipation rate ε and the standard deviation of radius σ and that R_T decreases rapidly with σ while disappearing at $\sigma > 3.5\,\mu$m. The LCM also reveals that σ and ε increase with time during the period of autoconversion, which helps to suppress the early precipitation by reducing A with smaller α and larger R_T in the initial stage. Finally, β is found to be affected by the accumulated collisional growth, which determines the drop size distribution.

1. Introduction

Warm cloud microphysical parameterizations usually divide the droplet spectrum within a cloud into cloud droplets and raindrops by size and calculates their physical quantities separately, following Kessler (1969, hereafter K69). Cloud droplets with small terminal velocity are assumed to remain within a cloud, and larger raindrops with appreciable terminal velocities are assumed to settle gravitationally, causing precipitation. The value of a separation radius r^* between cloud droplets and raindrops is in the range of 20–50 μm.

The mass transfer from cloud water to rainwater plays a critical role in the cloud microphysics parameterization, and it is divided into autoconversion, which results from the coalescence of cloud droplets, and accretion, which results from the coalescence of cloud droplets and raindrops. Autoconversion and accretion rates, A and C, respectively, can be thus expressed (Beheng and Doms 1986) as

$$A = \int_0^{x^*}\left[\int_{x^*-x}^{x^*} K(x,x')x'n(x')\,dx'\right]n(x)\,dx \qquad (1)$$

and

$$C = \int_{x^*}^{\infty}\left[\int_0^{x^*} K(x,x')x'n(x')\,dx'\right]n(x)\,dx, \qquad (2)$$

where $n(x)$ is the number concentration of drops with mass between x and $x + dx$, $x^* = (4/3)\rho\pi r^{*3}$, K is the collection kernel, and ρ is the density of water. A collision event that does not change the category of the involved droplets is called self-collection.

Numerous parameterizations have been suggested for autoconversion. One of the most widely used

Denotes content that is immediately available upon publication as open access.

[a] Current affiliation: Cooperative Institute for Research in Environmental Sciences, University of Colorado Boulder, and NOAA/Earth System Research Laboratory/Chemical Science Division, Boulder, Colorado.

Corresponding author: Yign Noh, noh@yonsei.ac.kr

DOI: 10.1175/JAS-D-18-0080.1

© 2018 American Meteorological Society. For information regarding reuse of this content and general copyright information, consult the AMS Copyright Policy (www.ametsoc.org/PUBSReuseLicenses).

parameterizations is the so-called Kessler-type parameterization, originally proposed by K69 as

$$A = \alpha q_c H(q_c - q_{cT}), \quad (3)$$

where q_c is the cloud water mixing ratio and H is the Heaviside step function. The proportional constant α and the threshold value q_{cT} are used typically as $\alpha = 10^{-3}\,\mathrm{s}^{-1}$ and $q_{cT} = 5 \times 10^{-4}$.

A more comprehensive expression was proposed by Manton and Cotton (1977) and Tripoli and Cotton (1980, hereafter TC80), which can be written as

$$A = \alpha q_c^{7/3} N_c^{-1/3} H(R - R_T), \quad (4)$$

with the empirical constant α. Here, the mean volume radius R is used to determine the threshold condition instead of q_c. The parameterization (4) can be obtained from (1) by assuming that $A \sim K N_c q_c$, $K \sim E R^2 V_T(R)$, and $V_T(R) \propto R^2$, based on the collection kernel K derived by Long (1974) and the terminal velocity of a droplet $V_T(R)$ at small R by the Stokes law, where N_c is the cloud droplet number concentration and E is the collection efficiency. TC80 suggested $\alpha = 38.56\,\mathrm{cm}^{-1}\,\mathrm{s}^{-1}$ by assuming $E = 0.55$. They also suggested $R_T = 10\,\mu\mathrm{m}$, but a smaller value is often used (Wood 2005). Liou and Ou (1989), Baker (1993), and Liu and Daum (2004) also suggested modified versions of the Kessler-type parameterization. Other functional forms of A that do not use the Kessler-type parameterization were also proposed (Berry and Reinhardt 1974; Beheng 1994, hereafter B94; Khairoutdinov and Kogan 2000, hereafter KK00; Seifert and Beheng 2001).

Meanwhile, various evidence suggests that autoconversion is also influenced by various other factors besides N_c and q_c, and attempts have been made to incorporate these factors into account. Seifert et al. (2010), Franklin (2008), and Seifert and Onishi (2016) attempted to include the effect of the turbulence-induced collection enhancement (TICE), that is, a larger K under the influence of turbulence compared to gravitational collisions. Berry and Reinhardt (1974), B94, Liu and Daum (2004), and Milbrandt and Yau (2005) considered the effect of the dispersion of the drop size distribution (DSD), which induces larger K by increasing the vertical velocity difference between two droplets. Meanwhile, Cotton and Anthes (1989) pointed out that the "aging period" is necessary to commence autoconversion in order to avoid the early production of rainwater too low in the cloud. Straka and Rasmussen (1997) attempted to include its effect in the parameterization. Similarly, Seifert and Beheng (2001) considered the internal time scale in their parameterization.

Accretion is usually parameterized by considering cloud droplets within a cylindrical volume swept out by a gravitationally settling raindrop while assuming a raindrop size distribution. The accretion rate C depends on raindrop mixing ratio q_r as well as q_c and is usually represented in the form as

$$C = \beta q_c^m q_r^n. \quad (5)$$

Typically, $m = n = 1$ is used (TC80; B94), although slightly different values are also used.

Autoconversion rates vary much more between schemes than accretion rates, often causing a difference by several orders of magnitude for the same q_c (Menon et al. 2003; Wood 2005; Hsieh et al. 2009). The contribution of accretion to total precipitation is much larger than that of autoconversion in general. Nonetheless, autoconversion still plays a critical role, because it generates initial raindrops required for accretion and subsequent precipitation. Accordingly, the proper parameterization of autoconversion still remains a key issue in cloud microphysics parameterization.

Considering the difficulty of obtaining reliable observation data, one valuable approach to evaluate cloud microphysics parameterizations is to analyze the results from a model that can simulate the variation of droplet spectrum directly, such as a spectral-bin model (SBM), which solves the stochastic collection equation (SCE). The results of the SBM initialized with observed DSD data (Wood 2005; Hsieh et al. 2009) or with the idealized DSD (Seifert and Beheng 2001; Franklin 2008; Lee and Baik 2017) were used to evaluate parameterizations of A and C. Meanwhile, KK00 and Kogan (2013) developed a formula for A and C from regression analysis of SBM data, when a stratocumulus or cumulus cloud is simulated by large-eddy simulation (LES). LES has an advantage of providing the dynamically balanced DSD within the fine structure of the cloud, which plays an important role in the calculation of A and C from (1) and (2) (Kogan 2013). Evaluations have been carried out usually by the comparison of A and C calculated from the SBM and the parameterization. However, the comparison can be affected by factors that are not represented in the parameterization, such as DSD, TICE, and aging time.

An Eulerian model, such as the SBM, calculates only the averaged values of A and C over the grid size and the time step. Moreover, the numerical diffusion of the droplet spectrum, in both physical and spectral space, can hinder the accurate calculation of A and C. Therefore, probably the ideal approach to calculate A and C is to capture the moment of each Lagrangian droplet growing to a raindrop together with the background condition, as suggested by Straka (2009). Nonetheless, it is possible only when cloud droplets are simulated by Lagrangian particles.

Recently, several groups developed Lagrangian cloud models (LCMs), in which the cloud microphysics of Lagrangian droplets and cloud dynamics are two-way coupled (e.g., Andrejczuk et al. 2010; Shima et al. 2009; Sölch and Kärcher 2010; Riechelmann et al. 2012; Hoffmann et al. 2017). In these models, the flow field is simulated by LES, and the droplets are treated as Lagrangian particles, which undergo cloud microphysics while interacting with the surrounding air.

Hoffmann et al. (2017) applied the LCM to clarify the mechanism of raindrop formation in a shallow cumulus cloud. They found that the rapid collisional growth, leading to raindrop formation, is triggered when droplets with a radius of 20 μm appear in the region near the cloud top that is characterized by large liquid water content, strong turbulence, large mean droplet size, a broad DSD, and high supersaturations. They also found that the rapid collisional growth leading to precipitation can be delayed without the broadening of the DSD, when turbulence is weak. On the other hand, TICE does not accelerate the triggering of the rapid collisional growth, but it enhances the collisional growth rate greatly after the triggering and thus results in faster and stronger precipitation. These results imply that both TICE and the dispersion of DSD are important factors to determine autoconversion and accretion.

The present paper aims to investigate the characteristics of the parameterizations of autoconversion and accretion by analyzing LCM data. For this purpose, we first compare A and C from the existing parameterizations with LCM data. At the next step, we investigate the effects of various other factors, such as the dispersion of the DSD, TICE, and aging time and parameterize their effects with an aim to improve the parameterization.

2. Simulation and analysis

a. Model description

The LCM in this study is coupled to the Parallelized Large-Eddy Simulation Model (PALM; Raasch and Schröter 2001; Maronga et al. 2015). To handle an extremely large number of droplets in a cloud, the concept of a superdroplet is introduced. Each superdroplet represents a large number of real droplets of identical features (e.g., their radius). The number of real droplets belonging to a superdroplet of radius r_n is called the "weighting factor" W_n, and the total mass of a superdroplet M_n is then calculated by

$$M_n = W_n \frac{4}{3}\pi\rho r_n^3. \tag{6}$$

In the present model, W_n differs for each superdroplet and changes with time as a result of collision and coalescence. The liquid water mixing ratio q_l for a given grid box of volume ΔV is then calculated by

$$q_l = \frac{1}{\rho_0 \Delta V}\sum_{n=1}^{N_P} M_n, \tag{7}$$

where ρ_0 is the density of dry air and N_P is the number of superdroplets in an LES grid box.

The velocity of each superdroplet is determined by

$$U_i = u_i + \tilde{u}_i - \delta_{i3}V_T(r), \tag{8}$$

where u_i is the LES resolved-scale velocity at the particle's location and $\tilde{u}_i$ is a stochastic turbulent velocity component $\tilde{u}_i$, computed in accordance with the LES subgrid-scale model (Sölch and Kärcher 2010). The terminal velocity V_T follows Rogers et al. (1993).

The diffusional growth of each superdroplet is calculated from

$$r_n \frac{dr_n}{dt} = \frac{S}{F_k + F_D} f(r_n), \tag{9}$$

where S is the supersaturation; F_k and F_D are the thermodynamic terms associated with heat conduction and vapor diffusion, respectively; and $f(r_n)$ represents the ventilation effect. Their functional forms follow Rogers and Yau (1989).

The temporal change of q_l due to condensation/evaporation is then calculated as

$$\left[\frac{dq_l}{dt}\right]_{\mathrm{Cond}} = \frac{\rho}{\rho_0 \Delta V}\sum_{n=1}^{N_p} W_n \frac{4\pi}{3}\frac{d}{dt} r_n^3, \tag{10}$$

and it determines the sink/source for potential temperature θ and water vapor mixing ratio q in the LES model.

To calculate the droplet growth by collision–coalescence, a statistical approach is used in which the growth of a superdroplet is calculated from the droplet spectrum resulting from all superdroplets currently located in the same grid box. The collisional growth is described in terms of the modification of W_n and M_n, which can be summarized as

$$\frac{dW_n}{dt}\delta t = -\frac{1}{2}(W_n - 1)P[K(r_n, r_n)W_n \delta t/\Delta V] - \sum_{m=n+1}^{N_P} W_m P[K(r_m, r_n)W_n \delta t/\Delta V], \tag{11}$$

$$\frac{dM_n}{dt}\delta t = \sum_{m=1}^{n-1} W_n \frac{M_m}{W_m} P\left[\frac{K(r_n, r_m)W_m \delta t}{\Delta V}\right] - \sum_{m=n+1}^{N_P} W_m \frac{M_n}{W_n} P\left[\frac{K(r_m, r_n)W_n \delta t}{\Delta V}\right], \tag{12}$$

assuming that the particles are sorted that $W_m > W_n$ for $n > m$. Here, the collection of a superdroplet pair with $W_m > W_n$ is realized by the collection of W_n droplets of the superdroplet m by the superdroplet n. It results in the decrease of W_m but no change of r_m, thus leading to the decrease of M_m [represented by the second terms in the rhs of (11) and (12)], and the increase of r_n but no change of W_n, thus leading to the increase of M_n [represented by the first term in the rhs of (12)]. The first term on the rhs of (11) describes the decrease of W_n due to internal collections of droplets within a superdroplet. If $\varphi > \xi$ in the probabilistic binary function $P[\varphi]$, where ξ is a random number uniformly chosen from the interval [0, 1], the collection takes place ($P[\varphi] = 1$). No collection takes place if $\varphi \le \xi$ ($P[\varphi] = 0$); $P[\varphi]$ is necessary to realize the stochastic collisional growth (Telford 1955). Small perturbation is given to the initial weighting factor of each superdroplet to help initiate the collision process. One can refer to Hoffmann et al. (2017) for the detailed explanation of the collision scheme. Unterstrasser et al. (2017) examined the performance of the present collision algorithm under various conditions, while comparing with analytical and SBM results, and confirmed that it can reproduce the realistic evolution of cloud droplet spectrum.

b. Simulation setup

The simulation setup is the same as in Hoffmann et al. (2017). A shallow cumulus cloud is triggered by a two-dimensional rising bubble of warm air, which is homogeneous in the x direction. The bubble is prescribed by an initial potential temperature difference θ^* given by

$$\theta^* = \theta_0^* \exp\left\{-\frac{1}{2}\left[\left(\frac{y-y_c}{a_y}\right)^2 + \left(\frac{z-z_c}{a_z}\right)^2\right]\right\}, \qquad (13)$$

where $y_c = 1920$ m and $z_c = 150$ m mark the center of the bubble, $a_y = 200$ m and $a_z = 170$ m the radius of the bubble, and $\theta_0^* = 0.4$ K, the maximum temperature difference. The model domain is 1920 m × 5760 m × 3840 m along the x, y, and z directions with an isotropic grid spacing of 20 m. Periodic boundary conditions are applied laterally, and Dirichlet and Neumann boundary conditions are applied at the bottom and top, respectively. The initial profiles of θ and q are derived from the LES intercomparison of shallow cumulus convection by vanZanten et al. (2011; Fig. 1 in Hoffmann et al. 2017). They represent the average thermodynamic state of a cumulus-topped boundary layer, as observed during the Rain in Cumulus over the Ocean (RICO) field campaign (Rauber et al. 2007). No background winds, no large-scale forcings, and no surface fluxes are applied.

The average distance between superdroplets is initially 3.4 m, yielding a total number of 7.9×10^8 superdroplets and about 200 superdroplets per grid box, which has been found to be sufficient to represent the collisional growth correctly (Riechelmann et al. 2012; Arabas and Shima 2013; Unterstrasser et al. 2017). Two different initial droplet number concentrations $N_0 = 70$ and 150 cm^{-3} are simulated by using $W_{n,\mathrm{init}} = 2.8 \times 10^9$ and 6.0×10^9. The radius of all superdroplets is initially given by $r = 0.01\,\mu$m, and the particles are not allowed to evaporate any smaller. A time step of $\Delta t = 0.2$ s is used in both LCM and LES.

Two simulations are carried out for each N_0 with different collection kernel K, which either considers only gravitational collision and coalescence (Hall 1980) or includes also the effect of TICE (Ayala et al. 2008; Wang and Grabowski 2009). In the latter case, TICE is parameterized as a function of the dissipation rate ε, which is calculated from the subgrid-scale model of LES. These simulations are called GRAV and TURB, respectively.

c. Calculation of autoconversion and accretion

First, we detect collision events during the time step Δt; that is, $P = 1$ in (11) and (12). The increased mass of a superdroplet n after a collision with other superdroplet m ($W_n < W_m$), ΔM_{mn}, is calculated for these droplets by

$$\Delta M_{mn} = W_n \frac{M_m}{W_m}. \qquad (14)$$

Every collision event is assigned to autoconversion, accretion, and self-collection, depending on the radii r_m and r_n before collision, and the radius r_n' after collision (Table 1). The case of accretion with $r_m > r^*$ and $r_n < r^*$ is possible in principle but negligible, because $r_n > r_m$ mostly occurs with $W_n < W_m$ after the initial period. The consequent mass transfer from cloud droplets to raindrops after a collision event is then calculated for autoconversion and accretion; that is, autoconversion is calculated by M_n' ($=M_n + \Delta M_{mn}$), and accretion is calculated by ΔM_{mn} for $r_n > r^*$ and M_n for $r_n < r^*$. The autoconversion and accretion rates at each grid box, A_i and C_i, respectively, can be obtained by adding up the contribution from every collision event belonging to the corresponding category of collision within a grid box per unit time. Only a very small fraction of superdroplets experience collision ($\Delta M_{mn} > 0$) during Δt (=0.2 s) in the simulation.

Here, the critical radius that separates a cloud droplet and a raindrop is given by $r^* = 25\,\mu$m. It is the same used by KK00 for shallow clouds. Larger values about 40–50 μm are often used for deep clouds (Berry and Reinhardt 1974; Seifert and Beheng 2001). Hoffmann et al. (2017) showed that the collisional growth, which

TABLE 1. Grouping of collision event to autoconversion, accretion, and self-collection (○: raindrop; ×: cloud droplet).

r_m	r_n	r'_n	Group
×	×	×	Self-collection
×	×	○	Autoconversion
×	○	○	Accretion
○	×	○	Accretion
○	○	○	Self-collection

generate autoconversion and accretion, starts as the droplet size reaches $r = 20\,\mu$m. It is therefore desirable to choose r^* that is slightly larger than 20 μm, considering that the collection of larger droplets should be characterized as accretion. Sensitivity of the results to r^* is examined in the next section.

Since most autoconversion parameterizations are expressed as a function of q_c, we calculate $A(q_c)$ by the following formula:

$$A(q_c) = \frac{1}{N_{q_c}} \sum_{i=1}^{N_{q_c}} A_i, \qquad (15)$$

where N_{q_c} is the number of grid boxes with q_c, using bins of a logarithmic width of $\Delta \log q_c = 0.0378$ within the cloud from the data obtained at every time step over the whole period of cloud evolution. The cloud is defined as the region where $q_l > 1.0 \times 10^{-5}\,\mathrm{kg\,kg^{-1}}$.

Similarly, we calculate the accretion rate C as a function of $q_c q_r$, as adopted in most formulas (TC80; B94; KK00); that is,

$$C(Q_{cr}) = \frac{1}{N_{Q_{cr}}} \sum_{i=1}^{N_{Q_{cr}}} C_i, \qquad (16)$$

where $Q_{cr} = q_c q_r$ and $N_{Q_{cr}}$ is the number of grids with Q_{cr} within a cloud. The bin width is $\Delta \log Q_{cr} = 0.0235$.

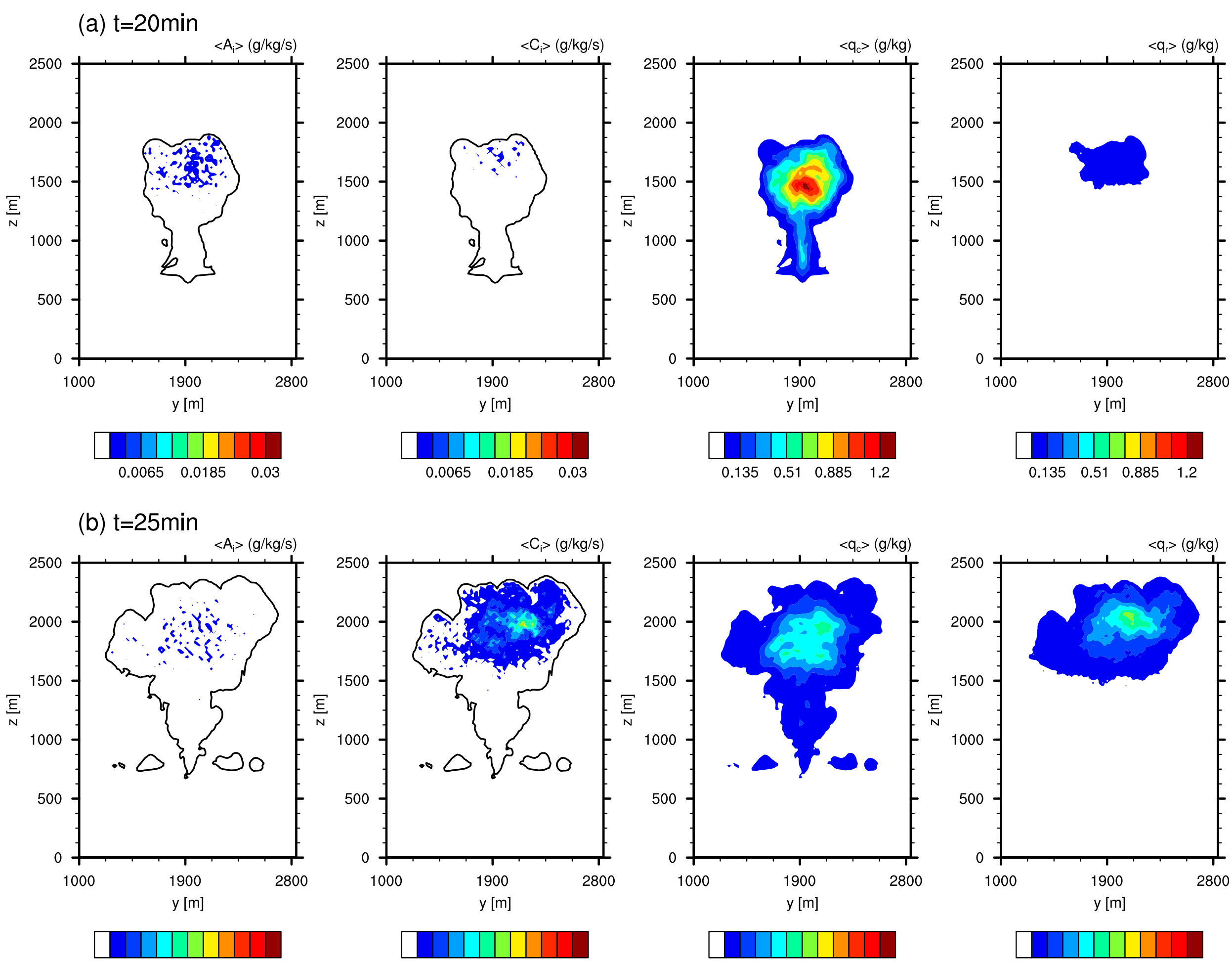

FIG. 1. Distributions of $\langle A_i \rangle$, $\langle C_i \rangle$, $\langle q_c \rangle$, and $\langle q_r \rangle$ (angle brackets mean the average over the x direction) at (a) t = 20 and (b) t = 25 min.

It should be mentioned that the calculations of A and C from the LCM and the SBM are somewhat different in nature. First, A and C are calculated by the integral of SCE within a grid in the SBM, but they are calculated at every collision event of Lagrangian droplets in the LCM. It also implies that they are affected by the growth history of Lagrangian droplets in the LCM. Second, the occurrence of autoconversion and accretion is continuous and deterministic in the SBM, but it is intermittent and stochastic in the LCM. Accordingly, the values of A_i and C_i are zero in a large number of grids in the LCM, contrary to the SBM.

3. Results

a. Distribution of autoconversion and accretion

Figure 1 shows the distributions of autoconversion, accretion, q_c, and q_r, averaged in the x direction, during the evolution of a cumulus cloud (t = 20 and 25 min).

Autoconversion is larger than accretion initially (t = 20 min), but accretion soon dominates the conversion to raindrops (t = 25 min). It also reveals that both autoconversion and accretion appear in the upper part of the cloud initially (t = 20 min), but they appear in the center in the later stage (t = 25 min). It reflects the fact that raindrop formation is triggered near the cloud top that is characterized by strong turbulence and a broad DSD (Hoffmann et al. 2017).

The dominance of autoconversion soon after the triggering of raindrop formation is clearly illustrated in the time series of the total amount of autoconversion and accretion per unit time within the cloud (Fig. 2a). As a result of autoconversion and accretion, q_c decreases and q_r increases (Fig. 2b). Ultimately, they disappear with time by precipitation and the dilution of the cloud. Both the time series of autoconversion and accretion and their distributions within a cloud are in agreement with previous results (Wood 2005; Franklin 2008).

Figure 2 also shows that both autoconversion and accretion are smaller in GRAV, although they start to appear at about the same time. It reflects the fact that TICE does not accelerate the timing of the raindrop formation, but it increases the amount of precipitation (Hoffmann et al. 2017). Seifert et al. (2010) also showed, using an SBM, that precipitation increases about 2 times, as ε increases from 0 to 100 cm^2 s^{-3}, when N_0 = 100 cm^{-3}.

b. Comparison of A and C with parameterizations

Figure 3 shows the variation of A with q_c from LCM results with different N_0 (=70 and 150 cm^{-3}) and collection kernels (GRAV, TURB). The frequency distribution q_c is also shown for reference; A is calculated

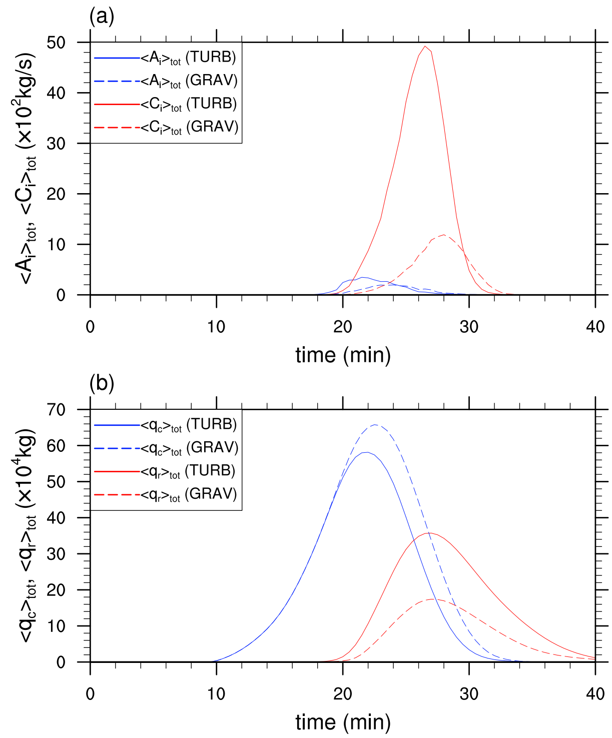

FIG. 2. Time series of cloud microphysical variables during the evolution of a cumulus cloud (angle brackets mean the total amount within the cloud; solid: TURB; dotted: GRAV) for (a) $\langle A_i \rangle_{tot}$ (blue) and $\langle C_i \rangle_{tot}$ (red) and (b) $\langle q_c \rangle_{tot}$ (blue) and $\langle q_r \rangle_{tot}$ (red).

only in the range where the number of grid boxes with q_c, N_{q_c}, is sufficiently large ($N_{q_c} > 5 \times 10^2$), since the frequency of collision events during Δt is very low. Autoconversion parameterizations by K69, TC80, B94, and KK00 are compared with LCM results, similar to Wood (2005) and Hsieh et al. (2009). Table 2 presents autoconversion and accretion formulations for the four parameterizations examined. In all schemes, we use N_0 for N_c. The N_c decreases by less than 20% during autoconversion ($t < 25$ min).

Remarkably, the results reproduce successfully the Kessler-type autoconversion parameterization, such as (3) and (4), in which the threshold q_c exists, and A increases with q_c. It reveals that autoconversion does not occur in a large volume of regions with small q_c within a cloud (Fig. 3). We should mention that the relation $A(q_c)$ has never been directly obtained so far. Previous works compared A from the parameterizations and SBMs (KK00; Seifert and Beheng 2001; Wood 2005; Franklin 2008; Hsieh et al. 2009; Kogan 2013; Lee and Baik 2017).

The closest agreement in the relation $A \propto q_c^\gamma$ is found with TC80; that is, $\gamma = 7/3$, although the values of α and R_T in (4) are different. The value of γ is certainly larger than $\gamma = 1$ (K69) and smaller than $\gamma = 3$ (Liu and Daum 2004)

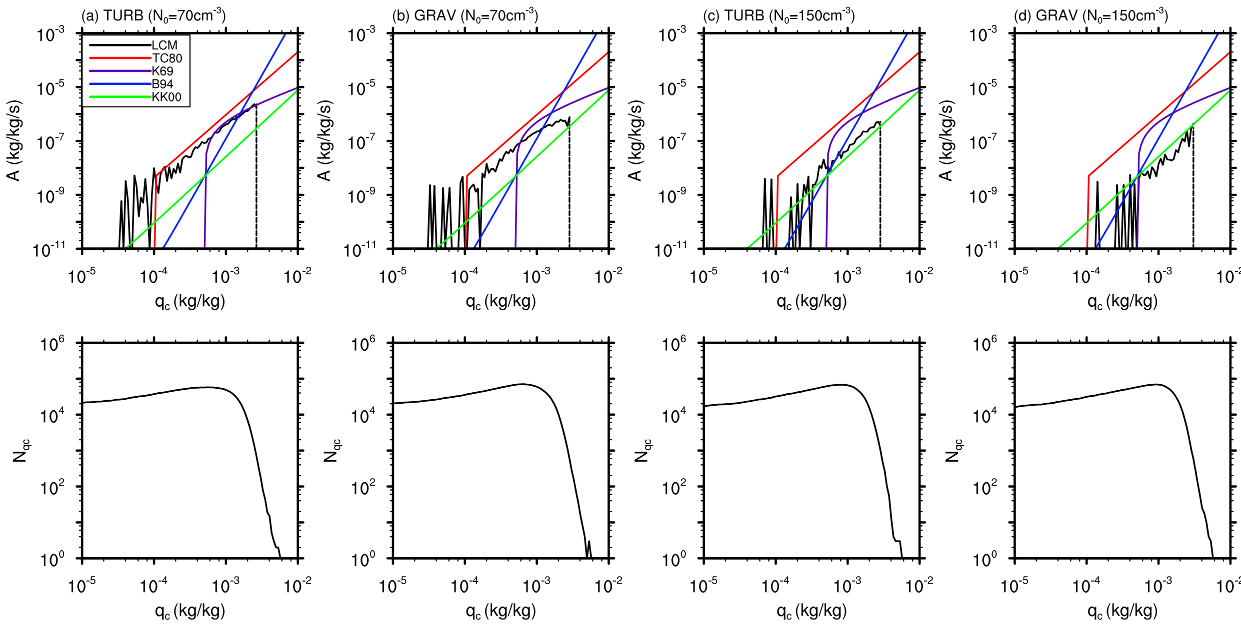

FIG. 3. Variation of (top) A and (bottom) N_{q_c} with q_c (black: LCM; red: TC80; violet: K69; blue: B94; green: KK00) for (a) TURB (N_0 = 70 cm^{-3}), (b) GRAV (N_0 = 70 cm^{-3}), (c) TURB (N_0 = 150 cm^{-3}), and (d) GRAV (N_0 = 150 cm^{-3}).

or $\gamma = 4.7$ (B94). A better agreement with TC80 is found for α in TURB and in smaller N_0, although it is always overestimated. It is consistent with previous reports that TC80 overestimates A from one to two orders of magnitude in the case of shallow cumulus clouds (Baker 1993; Wood 2005; Hsieh et al. 2009). Figure 3 also reveals many features that are consistent with previous assessments (Wood 2005; Hsieh et al. 2009). For example, B94 overestimates the increasing rate of A with q_c, and KK00 underestimates A except at low q_c below the threshold value. The threshold value and α are overestimated in K69. Considering that all previous comparisons are based on SBM data, the consistency with previous reports suggests the general agreement in the calculations of A and C from the LCM and the SBM.

Similarly, we examined the variation of C with Q_{cr} ($=q_c q_r$) from LCM results with different N_0 (=70 and 150 cm^{-3}) and collection kernels (GRAV and TURB; Fig. 4). Once again, the frequency distribution of Q_{cr} is displayed for reference, and C is calculated only in the range where the number of grids with Q_{cr} is sufficiently large ($N_{Q_{cr}} > 50$). Here, we consider only the schemes in which C varies with Q_{cr} (KK00; TC80; B94). The differences between accretion schemes are much smaller than between autoconversion schemes, similar to previous comparisons (KK00; Wood 2005; Hsieh et al. 2009). All show relatively good agreements with LCM results. Even the proportional constant β in $C = \beta Q_{cr}$ matches very well in GRAV, although it is somewhat larger in TURB. Meanwhile, C tends to increase slightly faster than Q_{cr} for $N_0 = 150$ cm^{-3}.

Finally, the sensitivity to r^* is examined by comparing the present results of A and C with those from $r^* = 40\,\mu$m (Fig. 5). No significant difference is observed, although the exponent γ in $A \propto q_c^\gamma$ is slightly smaller and the coefficient β in $C = \beta Q_{cr}$ is slightly larger. The closest agreement is still found with TC80.

TABLE 2. Autoconversion and accretion formulations for the four parameterizations examined (units are cm^{-3} for N_c).

Schemes	Autoconversion rate (kg kg^{-1} s^{-1})	Accretion rate (kg kg^{-1} s^{-1})
K69	$A = \alpha q_c H(q_c - q_{cT})$, where $\alpha = 10^{-3}$ and $q_{cT} = 5 \times 10^{-4}$	$C = \beta q_c q_r^{7/8} N_c^{1/8}$, where $\beta = 0.34$
TC80	$A = \alpha q_c^{7/3} N_c^{-1/3} H(R - R_T)$, where $\alpha = 38.56$ and $R_T = 7\,\mu$m	$C = \beta q_c q_r$, where $\beta = 5.83$
B94	$A = \alpha d^{-1.7} q_c^{4.7} N_c^{-3.3}$, where $\alpha = 9.33 \times 10^{14}$, $d = 9.9$ for $N_c < 200$ cm^{-3}, and $d = 3.9$ for $N_c > 200$ cm^{-3}	$C = \beta q_c q_r$, where $\beta = 7.2$
KK00	$A = \alpha q_c^{2.47} N_c^{-1.79}$, where $\alpha = 1350.0$	$C = \beta (q_c q_r)^{1.15}$, where $\beta = 67$

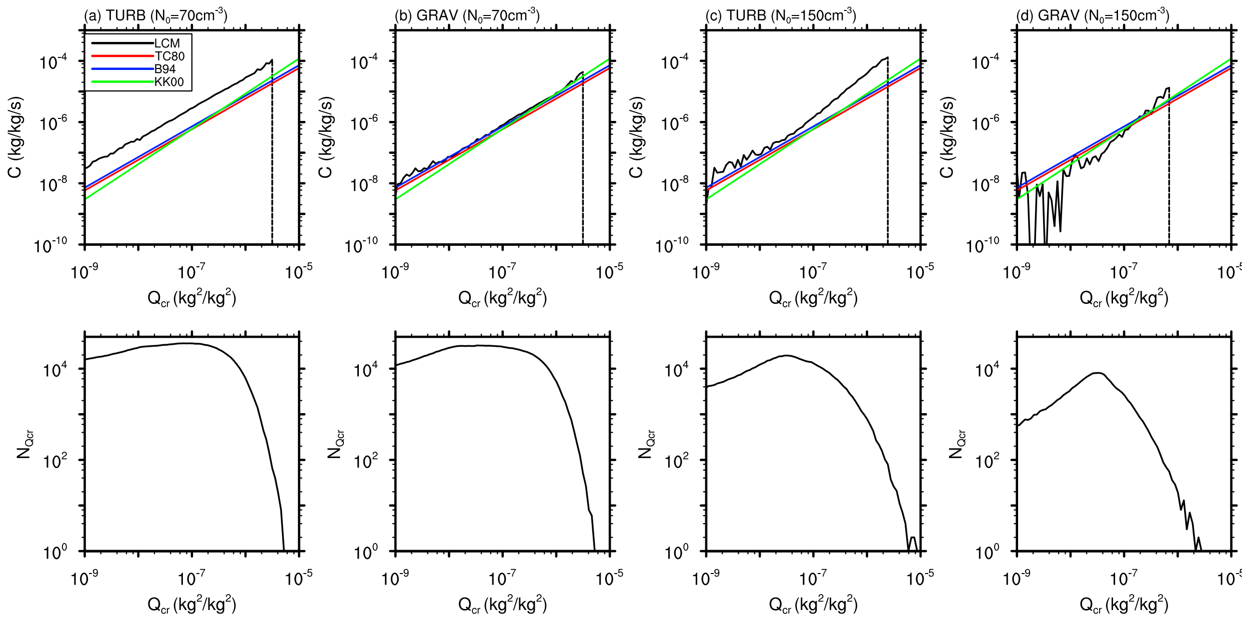

FIG. 4. Variation of (top) C and (bottom) $N_{Q_{cr}}$ with $Q_{cr}(=q_c q_r)$ (black: LCM; red: TC80; blue: B94; green: KK00) for (a) TURB (N_0 = 70 cm^{-3}), (b) GRAV (N_0 = 70 cm^{-3}), (c) TURB (N_0 = 150 cm^{-3}), and (d) GRAV (N_0 = 150 cm^{-3}).

c. *Influence of other factors on A and C*

As discussed in the introduction, various evidence indicates that autoconversion is influenced not only by q_c and N_c but also by various other factors, such as TICE, the dispersion of the DSD, and the aging time since the generation of a cloud.

To clarify the influences of these factors, we replot Fig. 3 based on the subgroup of data according to the values of the dissipation rate ε, the standard deviation of radius σ, and $t - t_0$, where t_0 is the time at which a cloud is generated at the lifting condensation level (LCL; =10 min; Fig. 6). Here, ε and σ represent the values in each grid box. If ε, σ, and $t - t_0$ are not sufficiently large, the autoconversion tends to be suppressed, resulting in smaller α and larger R_T. It is found that α is affected by all variables ε, σ, and $t - t_0$. On the other hand, R_T is affected only by σ and $t - t_0$ and insensitive to ε.

It is difficult, however, to identify the effects of ε, σ, and $t - t_0$ separately from the LCM results, because all variables vary simultaneously. For this purpose, we performed a large number of simulations of a simple box collision model, as in Hoffmann et al. (2017). Simulations were carried out under different ε (=0, 200, and 400 cm^2 s^{-3}), starting with lognormally distributed droplet spectra with different N_0 (=40, 70, and 150 cm^{-3}), σ (=0.5, 1.0, ..., 7.0 μm), and r_0 (=1, 2, ..., 18.0 μm), where r_0 is the arithmetic mean radius. The ranges of N_r/N_0 and q_c in the initial distributions are $N_r/N_0 < 0.2$ and $2.7 \times 10^{-8} < q_c < 1.47 \times 10^{-3}$. The collisional growth algorithm is the same as used in the LCM and represented by 200 superdroplets. The calculation of A is made only for the first time step ($\Delta t = 5$ s) so that we can assume that all initial variables remain unchanged.

There are at least five variables that can influence autoconversion, such as q_c, N_c, ε, σ, and t, and it makes it very difficult to identify their effects separately. Therefore, we assume the relation $A = \alpha q_c^{7/3} N_c^{-1/3}$ from (4) (TC80), based on Fig. 3. Analysis of data reveals that, when $\sigma > 3.5\,\mu$m, $A/(q_c^{7/3} N_c^{-1/3})$ does not vary significantly with r_0, and it never becomes smaller than 1/10 of its value at the largest r_0 (=18 μm), as r_0 decreases down to 1 μm (not shown). On the other hand, when $\sigma < 3.5\,\mu$m, $A/(q_c^{7/3} N_c^{-1/3})$ decreases rapidly with decreasing r_0. In this case, R_T is determined by the radius at which $A/(q_c^{7/3} N_c^{-1/3})$ becomes smaller than 1/10 of its value at the largest r_0 (=18 μm) for given ε and σ. The case with $\sigma > 3.5\,\mu$m is regarded as $R_T = 0\,\mu$m, that is, no threshold R. Finally, α is calculated by averaging $A/(q_c^{7/3} N_c^{-1/3})$ from the data with $\sigma > 3.5\,\mu$m for given ε and σ.

First, we examine how α and R_T are affected by N_c. Figure 7 shows that both α and R_T are essentially independent of N_0, or equivalently N_c, although they vary widely with σ and ε. Note that a large number of data with $\sigma > 3.5\,\mu$m belong to $R_T = 0\,\mu$m in Fig. 7b. Figure 7 also justifies the assumption of the relation $A = \alpha q_c^{7/3} N_c^{-1/3} H(R - R_T)$.

The variations of α and R_T with σ and ε are shown in Figs. 8 and 9 . They show that α increases with both σ and ε. On the other hand, R_T decreases rapidly with σ,

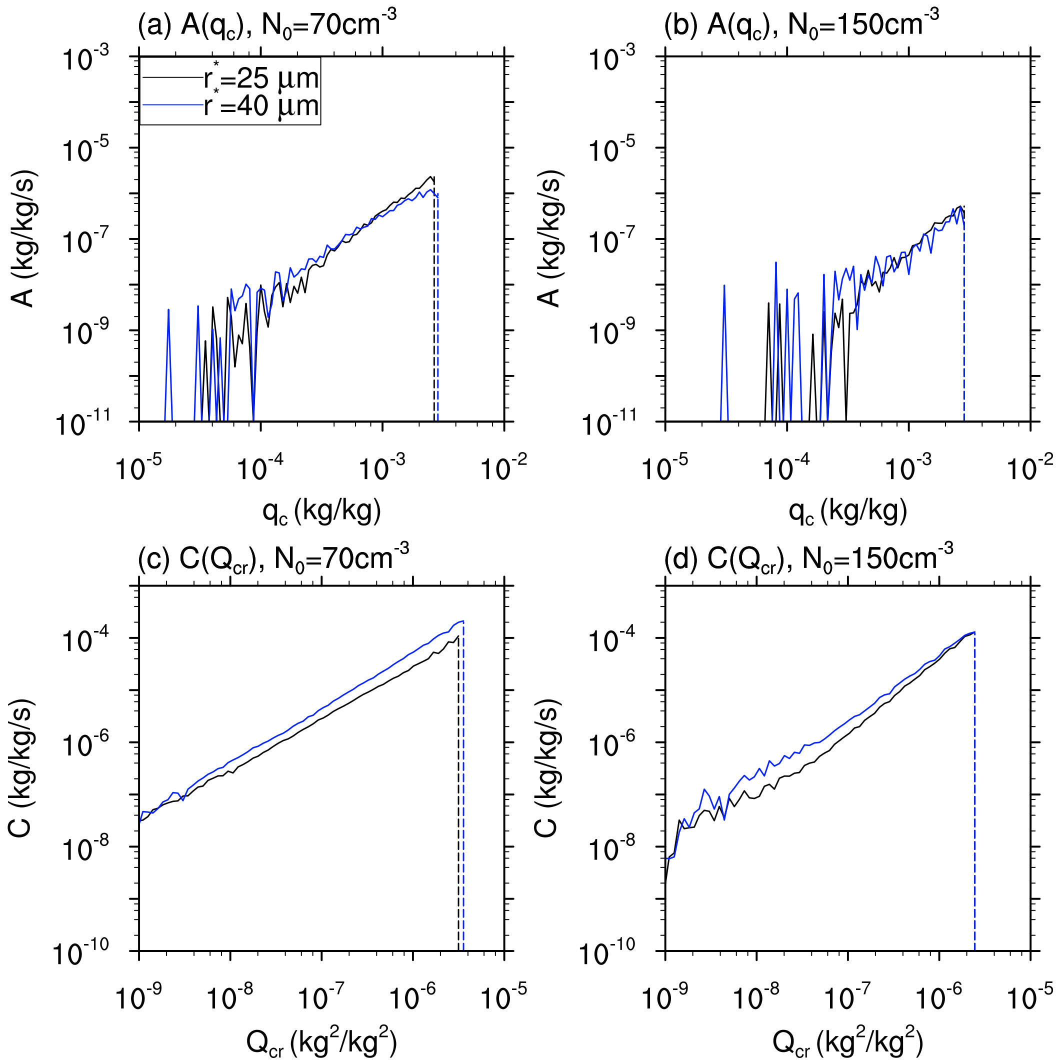

FIG. 5. Comparison of A and C from different r^* for TURB (black: $r^* = 25\,\mu$m; blue: $r^* = 40\,\mu$m) for (a) $A(q_c)$, $N_0 = 70\,\mathrm{cm}^{-3}$; (b) $A(q_c)$, $N_0 = 150\,\mathrm{cm}^{-3}$; (c) $C(Q_{cr})$, $N_0 = 70\,\mathrm{cm}^{-3}$; and (d) $C(Q_{cr})$, $N_0 = 150\,\mathrm{cm}^{-3}$.

and the threshold R disappears when $\sigma \geq 3.5\,\mu$m ($R_T = 0\,\mu$m). It also shows that R_T is insensitive to ε, although it tends to increase slightly for smaller ε. The increase of α with ε and σ and the decrease of R_T with σ are consistent with the dependence on ε and σ in Fig. 6.

We can obtain the dependence of α on σ and ε as

$$\alpha = a(\sigma - \sigma_\alpha)(1 + b\varepsilon), \tag{17}$$

with $a = 1.0\,\mathrm{cm}^{-1}\,\mu\mathrm{m}^{-1}\,\mathrm{s}^{-1}$, $b = 8.8 \times 10^{-3}\,\mathrm{cm}^{-2}\,\mathrm{s}^3$, and $\sigma_\alpha = 1.35\,\mu$m. The dependence of R_T on σ can be expressed as

$$R_T = \begin{cases} d_R^{1-m}(\sigma_R - \sigma)^m, & \sigma < \sigma_R \\ 0, & \sigma \geq \sigma_R, \end{cases} \tag{18}$$

where $\sigma_R = 3.5\,\mu$m, $m = 0.25$, and $d_R = 34.4\,\mu$m. According to (18), $R_T = 10\,\mu$m, employed by TC80, is expected at $\sigma \cong 3\,\mu$m, which is the typical value during the initial stage of shallow cumulus clouds (see Fig. 11 below).

The existence of the threshold R is attributed to two factors. First, if both R and σ are very small, the collection of two small droplets can never produce a droplet larger than r^*, regardless of N_c or q_c. Second, the rapid collisional growth is triggered when droplets larger than $r = 20\,\mu$m are present (Hoffmann et al. 2017). Therefore, if both R and σ are very small, very few droplets are larger than $r = 20\,\mu$m, and it makes the mean values of K very small.

Similar to the case of autoconversion, we replot Fig. 4 based on the data regrouped according to the values of ε, σ, and $t - t_0$ (Fig. 10). It shows that C tends to be larger for larger $t - t_0$ and σ, but it is rather insensitive to ε, as

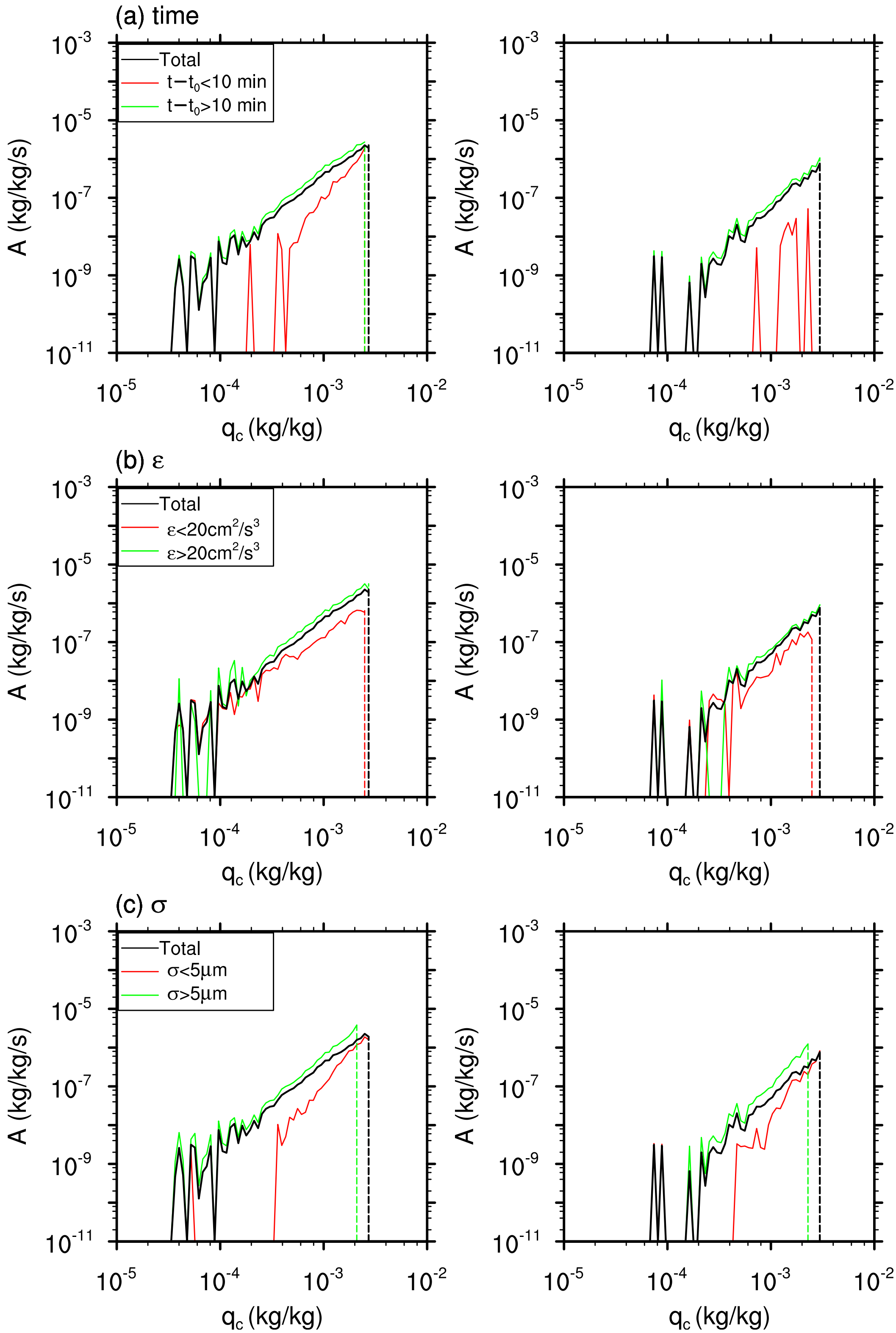

FIG. 6. Variation of A with q_c for different subgroups for TURB [(left) $N_0 = 70$ and (right) $N_0 = 150\,\mathrm{cm^{-3}}$]: (a) time (black: total; red: $t - t_0 < 10$ min; green: $t - t_0 > 10$ min), (b) ε (black: total; red: $\varepsilon < 20\,\mathrm{cm^2\,s^{-3}}$; green: $\varepsilon > 20\,\mathrm{cm^2\,s^{-3}}$), (c) σ (black: total; red: $\sigma < 5\,\mu$m; green: $\sigma > 5\,\mu$m).

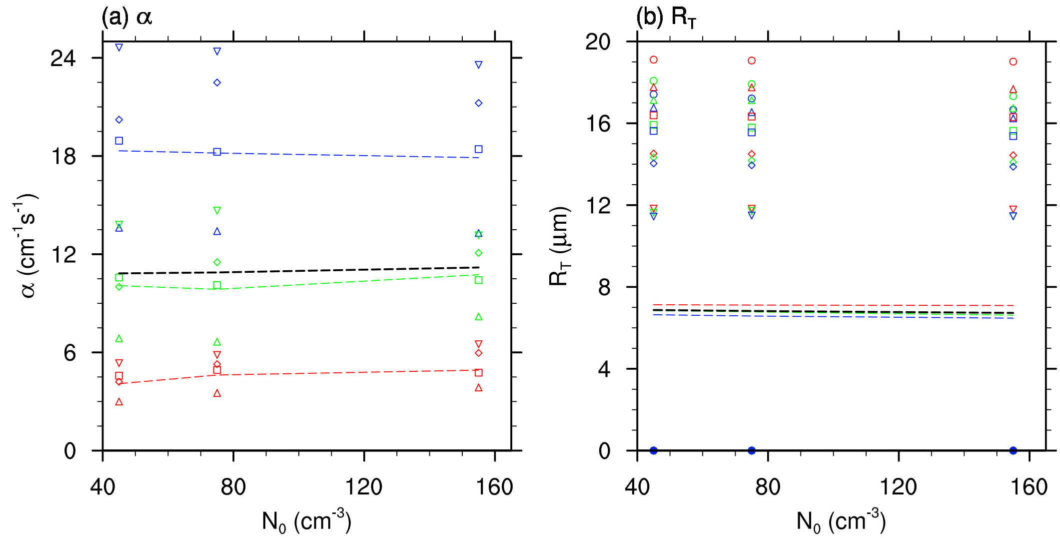

FIG. 7. Variations of α and R_T with N_0 from the box collision model. Here, results from the simulation with different ε and σ are represented by different color and symbols, respectively (red: $\varepsilon = 0\,\mathrm{cm^2\,s^{-3}}$; green: $\varepsilon = 200\,\mathrm{cm^2\,s^{-3}}$; blue: $\varepsilon = 400\,\mathrm{cm^2\,s^{-3}}$). The black dashed line represents the average of total simulation results for given N_0, and colored dashed lines represent the average of simulation results for given N_0 and ε: (a) α (triangle: $\sigma = 4\,\mu$m; square: $\sigma = 5\,\mu$m; diamond: $\sigma = 6\,\mu$m; inverted triangle: $\sigma = 7\,\mu$m) and (b) R_T (circle: $\sigma = 1\,\mu$m; triangle: $\sigma = 1.5\,\mu$m; square: $\sigma = 2\,\mu$m; diamond: $\sigma = 2.5\,\mu$m; inverted triangle: $\sigma = 3.0\,\mu$m). A large number of data are located at $R_T = 0\,\mu$m here.

expected from the dominance of gravitational collision for large droplets. It suggests that the larger C in TURB than in GRAV, shown in Fig. 4, is mainly due to the DSD with larger R and σ rather than the direct effect of TICE. The larger A under the influence of TICE produces more raindrops and, consequently, the larger DSD for raindrops. Actually, the mass density distributions of droplets (Fig. 7 in Hoffmann et al. 2017)

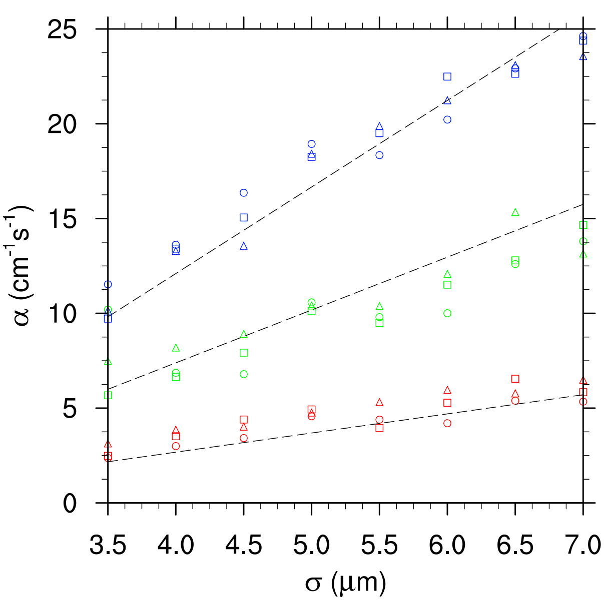

FIG. 8. Variations of α with σ from the box collision model together with the parameterization given by (17) (black dashed lines; red: $\varepsilon = 0\,\mathrm{cm^2\,s^{-3}}$; green: $\varepsilon = 200\,\mathrm{cm^2\,s^{-3}}$; blue: $\varepsilon = 400\,\mathrm{cm^2\,s^{-3}}$; circle: $N_0 = 40\,\mathrm{cm^{-3}}$; triangle: $N_0 = 70\,\mathrm{cm^{-3}}$; square: $N_0 = 150\,\mathrm{cm^{-3}}$).

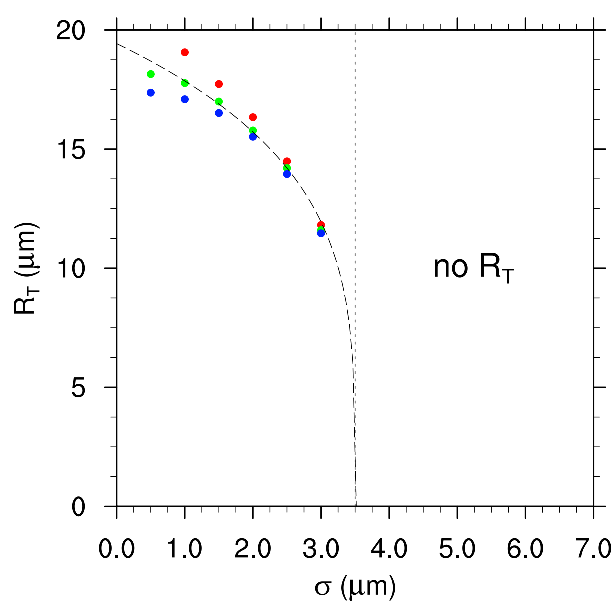

FIG. 9. Variations of R_T with σ from the box collision model together with the parameterization given by (18) (black dashed lines). The values of R_T are the same for all N_0 (red: $\varepsilon = 0\,\mathrm{cm^2\,s^{-3}}$; green: $\varepsilon = 200\,\mathrm{cm^2\,s^{-3}}$; blue: $\varepsilon = 400\,\mathrm{cm^2\,s^{-3}}$).

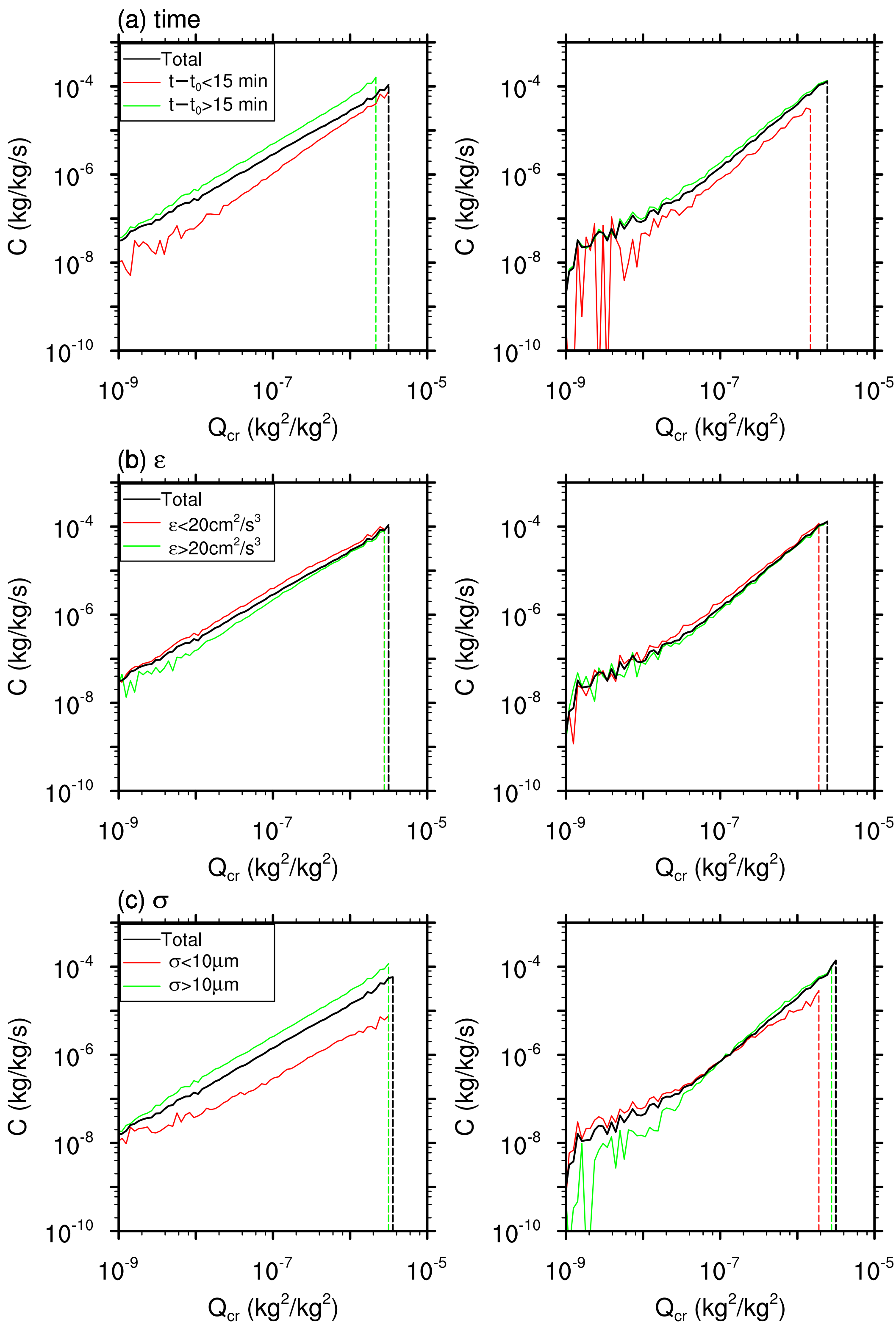

FIG. 10. Variation of C with Q_{cr} for different subgroups (TURB) with (left) $N_0 = 70$ and (right) $N_0 = 150\,\mathrm{cm}^{-3}$: (a) time (black: total; red: $t - t_0 < 15$ min; green: $t - t_0 > 15$ min), (b) ε (black: total; red: $\varepsilon < 20\,\mathrm{cm}^2\,\mathrm{s}^{-3}$; green: $\varepsilon > 20\,\mathrm{cm}^2\,\mathrm{s}^{-3}$), and (c) σ (black: total; red: $\sigma < 10\,\mu$m; green: $\sigma > 10\,\mu$m).

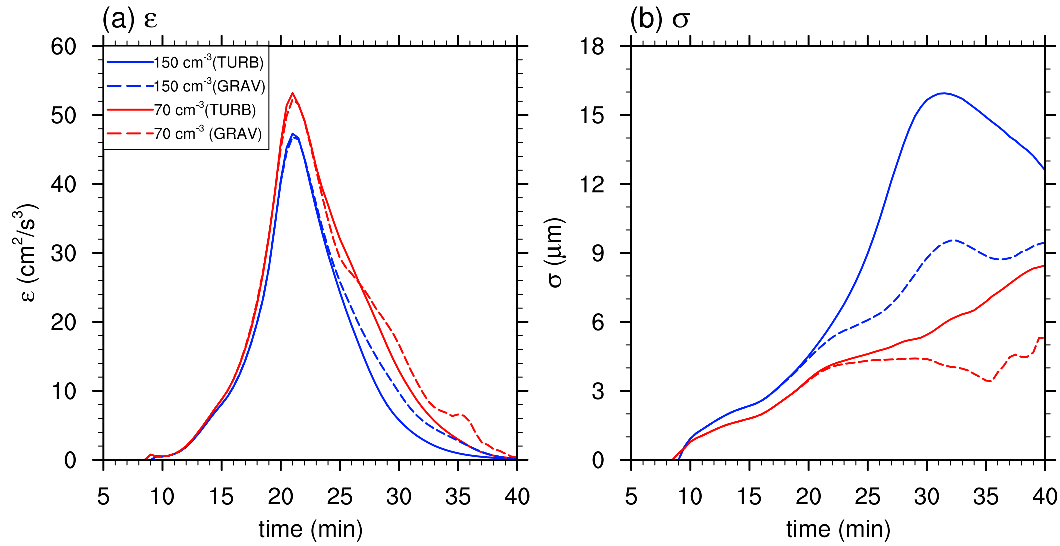

FIG. 11. Time series of the mean variables within a cloud (solid: TURB; dotted: GRAV; blue: $N_0 = 70\,\mathrm{cm}^{-3}$; red: $N_0 = 150\,\mathrm{cm}^{-3}$) for (a) ε and (b) σ.

exhibits larger R and σ in TURB than in GRAV after the collisional growth dominates ($t = 25$ min).

The broader DSD makes K larger in (2), thus producing larger accretion, even if Q_{cr} is the same. It means that β is affected by the accumulated contribution of the collisional growth, which determines the DSD. The narrower DSD also makes C smaller in the early stage (Fig. 10a).

d. Variations of ε and σ

We showed in the previous section that autoconversion varies significantly with ε and σ. The information of ε and σ is therefore necessary in order to apply the new autoconversion parameterization to a large-scale atmospheric model, such as a numerical weather prediction (NWP) model. However, ε and σ are not the variables that are usually predicted in most NWP models. Nonetheless, observational evidence indicates that the magnitudes of ε and σ vary widely during the evolution of a cloud and differ depending on the cloud type (Uijlenhoet et al. 2003; Hsieh et al. 2009; Geoffroy et al. 2010; Seifert et al. 2010).

With an aim to provide the information on the evolution of ε and σ for shallow cumulus clouds, we investigate how the mean values of ε and σ in an entire cloud vary with time (Fig. 11). It shows that both ε and σ increase with time after the generation of the cloud at $t = t_0$ (=10 min) at the LCL. After precipitation starts at $t = 21$ min (Fig. 2), ε decreases rapidly, but σ continues to increase for a while. The variation of ε is largely independent of N_0 and TICE until the initiation of precipitation, suggesting that they are mainly determined by cloud dynamics, insensitive to cloud microphysics. TICE makes σ larger after the initiation of precipitation because of the enhanced raindrop formation (Hoffmann et al. 2017). On the other hand, σ is smaller for larger N_0. Larger N_0 suppresses not only the condensational growth of droplets but also the broadening of the DSD, as reported earlier (Thompson et al. 2008; Hudson et al. 2012; Chandrakar et al. 2016).

The aging process is naturally realized by the initial increase of ε and σ with t, combined with the dependence of α and R_T on ε and σ. Small values of ε and σ in the early stage make α small and R_T large and thus suppress autoconversion, as shown in Fig. 6a. It can help avoid the too-early production of rainwater too low in the cloud, which is common in existing parameterizations (Cotton and Anthes 1989).

Another approach to estimate ε and σ is to use the information on the known parameters, such as q_c and N_c, if correlation exists between them (e.g., Geoffroy et al. 2010). Figure 12 shows two-dimensional histograms of the frequencies of ε–q_c and σ–q_c for the periods $t - t_0 < 10$ min and $t - t_0 > 10$ min. It reveals the negative correlation between σ and q_c and the positive correlation between ε and q_c at the late stage ($t - t_0 >$ 10 min). The positive correlation between ε and q_c reflects the fact that both ε and q_c are the largest in the cloud core near the top (e.g., Seifert et al. 2010). On the other hand, entrainment and mixing decrease q_c but increase σ near the cloud edge, leading to the negative correlation between σ and q_c. One can refer to the corresponding distributions of q_l, ε, and σ in Figs. 2 and 3 in Hoffmann et al. (2017). Figure 12 also reveals that the

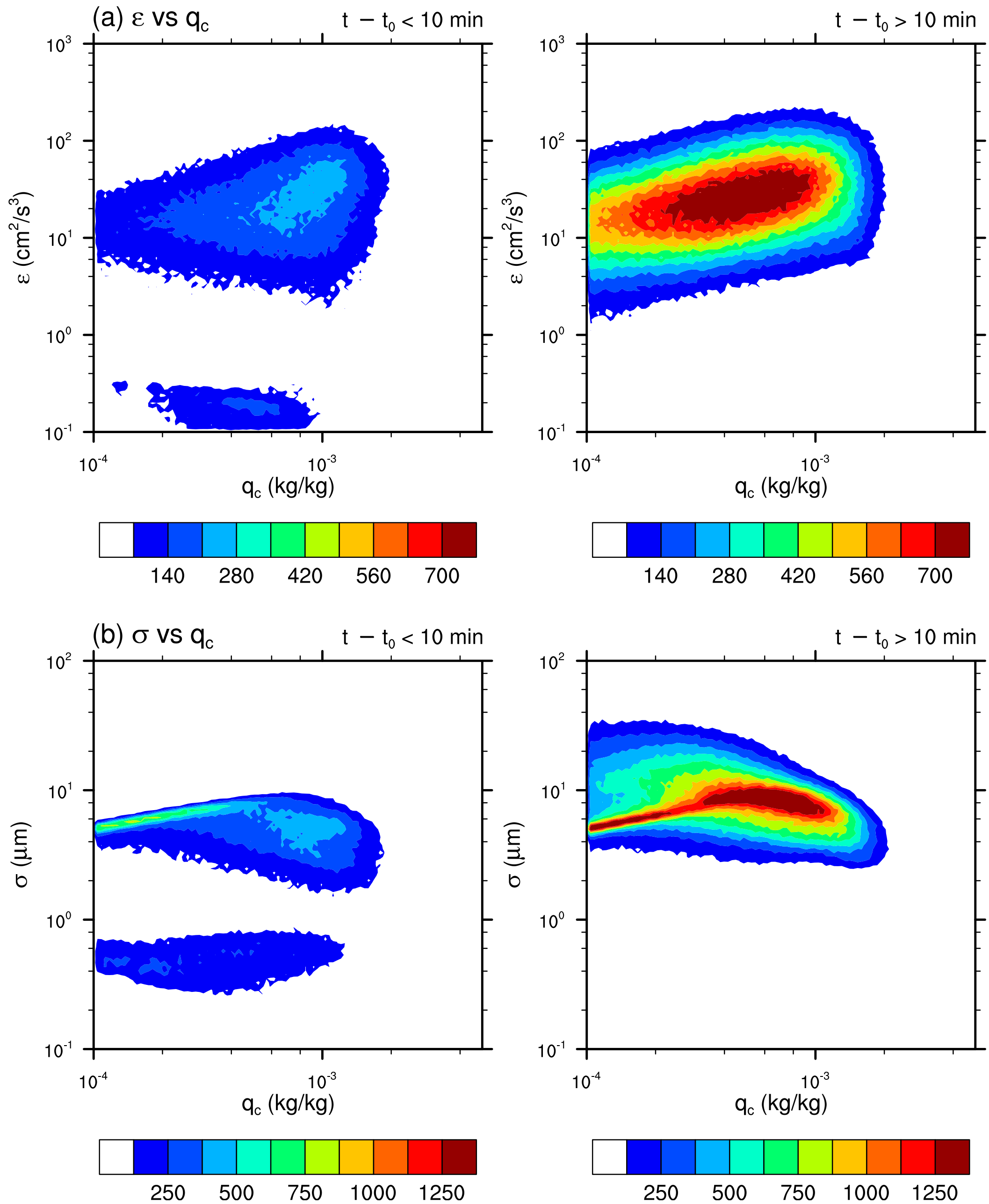

FIG. 12. Histograms of the number of grids in the (a) ε–q_c and (b) σ–q_c domains ($\Delta\log\varepsilon = 3.74\times10^{-2}\,\mathrm{cm^2\,s^{-3}}$, $\Delta\log\sigma = 3.03\times10^{-2}\,\mu\mathrm{m}$, and $\Delta\log q_c = 1.72\times10^{-2}\,\mathrm{kg\,kg^{-1}}$; $N_0 = 70\,\mathrm{cm^{-3}}$; TURB) at (left) $t - t_0 < 10$ and (right) $t - t_0 > 10\,\mathrm{min}$.

mean values of ε and σ in the late stage are larger than in the early stage, as expected from Fig. 11.

Contrary to the box collision model, in which ε, σ, and q_c are independent variables, they can be correlated with each other in the LCM. The correlations can affect the exponent γ in the relation $A \propto q_c^{\gamma}$, because α varies with q_c in (4). However, the opposite tendency in the variations of ε and σ with q_c (Fig. 12) may make the effects of ε and σ weak in the LCM results in the late stage ($t - t_0 > 10\,\mathrm{min}$). As a result, the relation $A \propto q_c^{7/3}$ can be maintained in the late stage (Fig. 6a) and also over the whole period (Fig. 3), since the number of data with $q_c > 10^{-4}\,\mathrm{kg\,kg^{-1}}$ is much larger in the late stage (Fig. 12). If the effects of ε and σ are not cancelled out, the relations $A \propto q_c^{7/3}$ will not be followed as shown in the cases with small $t - t_0$ and σ in Fig. 6.

TABLE 3. Comparison of TC80 and a new parameterization [$a = 1.0\,\mathrm{cm}^{-1}\,\mu\mathrm{m}^{-1}\,\mathrm{s}^{-1}$, $b = 8.8\times10^{-3}\,\mathrm{cm}^{-2}\,\mathrm{s}^{3}$, $\sigma_\alpha = 1.35\,\mu\mathrm{m}$, $m = 0.25$, $d_R = 34.4\,\mu\mathrm{m}$, $\sigma_R = 3.5\,\mu\mathrm{m}$, and t_0 is the time of cloud generation (=10 min)].

	TC80	New parameterization
Autoconversion: $A = \alpha q_c^{7/3} N_c^{-1/3} H(R - R_T)$	$\alpha = 38.56\,\mathrm{cm}^{-1}\,\mathrm{s}^{-1}$ $R_T = 10\,\mu\mathrm{m}$	$\alpha = a(\sigma - \sigma_\alpha)(1 + b\varepsilon)$ $R_T = \begin{cases} d_R^{1-m}(\sigma_R - \sigma)^m, & \sigma < \sigma_R \\ 0, & \sigma \ge \sigma_R \end{cases}$ $\varepsilon = \varepsilon(t - t_0, q_c)$ $\sigma = \sigma(t - t_0, q_c, N_0)$
Accretion: $C = \beta q_c q_r$	$\beta = 5.83$	$\beta = 6.3$–29.0

The previous parameterizations only in terms of q_c and N_c, as shown in Table 2, can be thought to be based on the assumption that the effects of the realistic distributions of ε and σ are already included implicitly. It is therefore possible that the different γ in other parameterizations may reflect the different variations of ε and σ with q_c depending on the cloud type. For example, Kogan (2013) found that the optimum γ is different depending on the cloud type (shallow cumulus clouds vs stratocumulus clouds). Nonetheless, the parameterizations neglecting the effects of ε and σ are unlikely to realize the aging effect.

4. Conclusions

In the present paper, we applied the LCM to investigate the cloud microphysics parameterization for shallow cumulus clouds, focusing on autoconversion and accretion. Autoconversion and accretion were calculated directly by capturing the moment of the conversion of individual Lagrangian droplets from cloud droplets to raindrops.

The autoconversion rate A and the accretion rate C, calculated from the LCM, were compared with various parameterizations (K69; TC80; B94; KK00). The calculation produced for the first time the formulas of autoconversion and accretion, such as $A(q_c)$ and $C(q_c q_r)$. The closest agreement is found with TC80, such as $A = \alpha N_c^{-1/3} q_c^{7/3} H(R - R_T)$ and $C = \beta q_c q_r$, although coefficients α, R_T, and β are different.

Furthermore, LCM results help to clarify how α and R_T are affected by the dissipation rate ε, the standard deviation of radius σ, and the age of the cloud $t - t_0$. The value of α is found to increase linearly with ε and σ. On the other hand, R_T decreases rapidly with σ, and it disappears as σ becomes larger than $3.5\,\mu$m. The effects of ε and σ on α and R_T are parameterized (Table 3). The LCM data also reveal that the values of σ and ε increase with time, during which autoconversion contributes significantly to the conversion to raindrops. It helps avoid the early precipitation, which is common in existing cloud microphysics parameterizations, because small α and large R_T, resulting from small ε and σ, suppress autoconversion. Accretion generally follows the expression $C = \beta q_c q_r$ well, but β tends to be larger than suggested by TC80, especially when TICE is included. The increase of C under TICE is due to larger R and σ as a result of accumulated contribution of collisional growth rather than the direct effect of TICE, however.

It is important to mention that (1) and (2) to calculate A and C are universal, independent of cloud dynamics and nucleation. Cloud dynamics and nucleation affect the variation of turbulence and DSD, and their effects are realized only in terms of the variation of K and n in (1) and (2) through the variation of ε and σ. We obtained the formula for the parameterization of A, including the dependence on ε and σ, by analyzing a large number of box collision model results with wide ranges of independent variables ε, σ, N_0, and r_0. It implies that the formula for A with the dependence on ε and σ in Table 3 is independent of the cloud type. On the other hand, the temporal evolutions of ε and σ in A and β in C may vary depending on the cloud type. If ε and σ are correlated with q_c in the real cloud, A can modify γ in the relation $A \propto q_c^\gamma$ because α in (4) varies with q_c. It is possible that the different γ in other parameterizations (Table 3) reflect the different variations of ε and σ with q_c under different cloud conditions. In our LCM results of a shallow cumulus cloud, the positive correlation between ε and q_c and the negative correlation between σ and q_c tend to cancel out their effects, and the relation $A \propto q_c^{7/3}$ is still observed.

We hope that an improved cloud microphysics parameterization, which takes into account the effect of the dispersion of DSD, TICE, and aging time, can be developed in the future based on the information obtained from the present work. It will be necessary for the application of the parameterization, however, to develop a general method to predict the variation of ε and σ by using the variables that are calculated in the NWP model, such as $t - t_0$, q_c, and N_c. Empirical constants, especially β, may need optimization too, which depends not only on the cloud type but also on the resolution and scales of the NWP. The optimal parameterization can be obtained by examining a large number of NWP simulation results. The more realistic simulations also help us to obtain further information on ε, σ, and β: for example, the inclusion of nucleation process, the inclusion of droplet breakup, cloud field simulations, and simulations under different thermodynamic sounding.

Acknowledgments. This work was funded by the Korea Meteorological Administration Research and Development Program under Grants KMI 2015-10410 and KMI 2018-07210. This LES/LCM used in this study (revision 1891) is publicly available (https://palm.muk.uni-hannover.de/trac/browser/palm?rev=1891). For analysis, the model has been extended, and additional analysis tools have been developed. The code is available from the authors on request. Most of the simulations have been carried out on the Cray XC-30 systems of the North-German Supercomputing Alliance (HLRN) and the supercomputer system supported by the National Center for Meteorological Supercomputer of Korea Meteorological Administration (KMA).

REFERENCES

Andrejczuk, M., W. W. Grabowski, J. Reisner, and A. Gadian, 2010: Cloud–aerosol interactions for boundary layer stratocumulus in the Lagrangian cloud model. *J. Geophys. Res.*, **115**, D22214, https://doi.org/10.1029/2010JD014248.

Arabas, S., and S. Shima, 2013: Large-eddy simulation of trade wind cumuli using particle-based microphysics with Monte Carlo coalescence. *J. Atmos. Sci.*, **70**, 2768–2777, https://doi.org/10.1175/JAS-D-12-0295.1.

Ayala, O., B. Rosa, L. P. Wang, and W. Grabowski, 2008: Effects of turbulence on the geometric collision rate of sedimenting droplets. Part 2. Theory and parameterization. *New J. Phys.*, **10**, 075016, https://doi.org/10.1088/1367-2630/10/7/075016.

Baker, M. B., 1993: Variability in concentration of cloud condensation nuclei in the marine cloud–topped boundary layer. *Tellus*, **45B**, 458–472, https://doi.org/10.3402/tellusb.v45i5.15742.

Beheng, K. D., 1994: A parameterization of warm microphysical conversion processes. *Atmos. Res.*, **33**, 193–206, https://doi.org/10.1016/0169-8095(94)90020-5.

——, and G. Doms, 1986: A general formulation of collection rates of cloud and raindrops using the kinetic equation and comparison with parameterizations. *Beitr. Phys. Atmos.*, **59**, 66–84.

Berry, E. X., and R. L. Reinhardt, 1974: An analysis of cloud drop growth by collection. Part II. Single initial distributions. *J. Atmos. Sci.*, **31**, 1825–1831, https://doi.org/10.1175/1520-0469(1974)031<1825:AAOCDG>2.0.CO;2.

Chandrakar, K. K., W. Cantrell, K. Chang, D. Ciochetto, D. Niedermeier, M. Ovchinnikov, R. A. Shaw, and F. Yang, 2016: Aerosol indirect effect from turbulence-induced broadening of cloud-droplet size distributions. *Proc. Natl. Acad. Sci. USA*, **113**, 14 243–14 248, https://doi.org/10.1073/pnas.1612686113.

Cotton, W. R., and R. A. Anthes, 1989: *Storm and Cloud Dynamics.* Academic Press, 883 pp.

Franklin, C. N., 2008: A warm rain microphysics parameterization that includes the effect of turbulence. *J. Atmos. Sci.*, **65**, 1795–1815, https://doi.org/10.1175/2007JAS2556.1.

Geoffroy, O., J.-L. Brenguier, and F. Burtnet, 2010: Parametric representation of the cloud droplet spectra for LES warm bulk microphysical schemes. *Atmos. Chem. Phys.*, **10**, 4835–4848, https://doi.org/10.5194/acp-10-4835-2010.

Hall, W. D., 1980: A detailed microphysical model within a two-dimensional dynamical framework: Model description and preliminary results. *J. Atmos. Sci.*, **37**, 2486–2507, https://doi.org/10.1175/1520-0469(1980)037<2486:ADMMWA>2.0.CO;2.

Hoffmann, F., Y. Noh, and S. Raasch, 2017: The route to raindrop formation in a shallow cumulus cloud simulated by a Langrangian cloud model. *J. Atmos. Sci.*, **74**, 2125–2142, https://doi.org/10.1175/JAS-D-16-0220.1.

Hsieh, W. C., H. Jonsson, L.-P. Wang, G. Buzorious, R. C. Flagan, J. H. Seinfield, and A. Nenes, 2009: On the representation of droplet coalescence and autoconversion: Evaluation using ambient cloud droplet size distribution. *J. Geophys. Res.*, **114**, D07201, https://doi.org/10.1029/2008JD010502.

Hudson, J. G., S. Noble, and V. Jha, 2012: Cloud droplet spectral width relationship to CCN spectra and vertical velocity. *J. Geophys. Res.*, **117**, D11211, https://doi.org/10.1029/2012JD017546.

Kessler, E., 1969: *On the Distribution and Continuity of Water Substance in Atmospheric Circulations. Meteor. Monogr.*, No. 10, Amer. Meteor. Soc., 84 pp.

Khairoutdinov, M., and Y. Kogan, 2000: A new cloud physics parameterization in a large-eddy simulation model of marine stratocumulus. *Mon. Wea. Rev.*, **128**, 229–243, https://doi.org/10.1175/1520-0493(2000)128<0229:ANCPPI>2.0.CO;2.

Kogan, Y., 2013: A cumulus cloud microphysics parameterization for cloud-resolving models. *J. Atmos. Sci.*, **70**, 1423–1436, https://doi.org/10.1175/JAS-D-12-0183.1.

Lee, H., and J.-J. Baik, 2017: A physically based autoconversion parameterization. *J. Atmos. Sci.*, **74**, 1599–1616, https://doi.org/10.1175/JAS-D-16-0207.1.

Liou, K.-N., and S.-C. Ou, 1989: The role of cloud microphysical processes in climate: An assessment from a one-dimensional perspective. *J. Geophys. Res.*, **94**, 8599–8607, https://doi.org/10.1029/JD094iD06p08599.

Liu, Y., and P. H. Daum, 2004: Parameterization of the autoconversion process. Part I: Analytical formulation of the Kessler-type parameterizations. *J. Atmos. Sci.*, **61**, 1539–1548, https://doi.org/10.1175/1520-0469(2004)061<1539:POTAPI>2.0.CO;2.

Long, A. B., 1974: Solutions to the droplet collection equation for polynomial kernels. *J. Atmos. Sci.*, **31**, 1040–1051, https://doi.org/10.1175/1520-0469(1974)031<1040:STTDCE>2.0.CO;2.

Manton, M. J., and W. R. Cotton, 1977: Formulation of approximate equations for modeling moist deep convection on the mesoscale. Colorado State University Dept. of Atmospheric Science Paper 266, 62 pp.

Maronga, B., and Coauthors, 2015: The Parallelized Large-Eddy Simulation Model (PALM) version 4.0 for atmospheric and oceanic flows: Model formulation, recent developments, and future perspectives. *Geosci. Model Dev.*, **8**, 2515–2551, https://doi.org/10.5194/gmd-8-2515-2015.

Menon, S., and Coauthors, 2003: Evaluating aerosol/cloud/radiation process parameterizations with single-column models and Second Aerosol Characterization Experiment (ACE-2) cloudy column observations. *J. Geophys. Res.*, **108**, 4762, https://doi.org/10.1029/2003JD003902.

Milbrandt, J. A., and M. K. Yau, 2005: A multimoment bulk microphysics parameterization. Part I: Analysis of the role of the spectral shape parameter. *J. Atmos. Sci.*, **62**, 3051–3064, https://doi.org/10.1175/JAS3534.1.

Raasch, S., and M. Schröter, 2001: PALM—A large-eddy simulation model performing on massively parallel computers. *Meteor. Z.*, **10**, 363–372, https://doi.org/10.1127/0941-2948/2001/0010-0363.

Rauber, R. M., and Coauthors, 2007: Rain in Shallow Cumulus over the Ocean: The RICO campaign. *Bull. Amer. Meteor. Soc.*, **88**, 1912–1928, https://doi.org/10.1175/BAMS-88-12-1912.

Riechelmann, T., Y. Noh, and S. Raasch, 2012: A new method for large-eddy simulations of clouds with Lagrangian droplets including the effects of turbulent collision. *New J. Phys.*, **14**, 065008, https://doi.org/10.1088/1367-2630/14/6/065008.

Rogers, R. R., and M. K. Yau, 1989: *A Short Course in Cloud Physics.* 3rd ed. Pergamon Press, 304 pp.

——, D. Baumgardner, S. Ethier, D. Carter, and W. Ecklund, 1993: Comparison of raindrop size distributions measured by radar wind profiler and by airplane. *J. Appl. Meteor.*, **32**, 694–699, https://doi.org/10.1175/1520-0450(1993)032<0694:CORSDM>2.0.CO;2.

Seifert, A., and K. D. Beheng, 2001: A double-moment parameterization for simulating autoconversion, accretion, and selfcollection. *Atmos. Res.*, **59–60**, 265–281, https://doi.org/10.1016/S0169-8095(01)00126-0.

——, and R. Onishi, 2016: Turbulence effects on warm-rain formation in precipitating shallow convection revisited. *Atmos. Chem. Phys.*, **16**, 12 127–12 141, https://doi.org/10.5194/acp-16-12127-2016.

——, L. Nuijens, and B. Stevens, 2010: Turbulence effects on warm-rain autoconversion in precipitating shallow convection. *Quart. J. Roy. Meteor. Soc.*, **136**, 1753–1762, https://doi.org/10.1002/qj.684.

Shima, S., K. Kusano, A. Kawano, T. Sugiyama, and S. Kawahara, 2009: The super-droplet method for the numerical simulation of clouds and precipitation: A particle-based and probabilistic microphysics model coupled with a non-hydrostatic model. *Quart. J. Roy. Meteor. Soc.*, **135**, 1307–1320, https://doi.org/10.1002/qj.441.

Sölch, I., and B. Kärcher, 2010: A large-eddy model for cirrus clouds with explicit aerosol and ice microphysics and Lagrangian ice particle tracking. *Quart. J. Roy. Meteor. Soc.*, **136**, 2074–2093, https://doi.org/10.1002/qj.689.

Straka, J. M., 2009: *Cloud and Precipitation Microphysics: Principles and Parameterizations.* Cambridge University Press, 384 pp.

——, and E. N. Rasmussen, 1997: Toward improving microphysical parameterizations of conversion processes. *J. Appl. Meteor.*, **36**, 896–902, https://doi.org/10.1175/1520-0450(1997)036<0896:TIMPOC>2.0.CO;2.

Telford, J., 1955: A new aspect of coalescence theory. *J. Meteor.*, **12**, 436–444, https://doi.org/10.1175/1520-0469(1955)012<0436:ANAOCT>2.0.CO;2.

Thompson, G., P. R. Field, R. M. Rasmussion, and W. D. Hall, 2008: Explicit forecasts of winter precipitation using an improved bulk microphysics scheme. Part II: Implementation of a new snow parameterization. *Mon. Wea. Rev.*, **136**, 5095–5116, https://doi.org/10.1175/2008MWR2387.1.

Tripoli, G. J., and W. R. Cotton, 1980: A numerical investigation of several factors contributing to the observed variable intensity of deep convection over south Florida. *J. Appl. Meteor.*, **19**, 1037–1063, https://doi.org/10.1175/1520-0450(1980)019<1037:ANIOSF>2.0.CO;2.

Uijlenhoet, R., M. Steiner, and J. A. Smith, 2003: Variability of raindrop size distributions in a squall line and implications for radar rainfall estimation. *J. Hydrometeor.*, **4**, 43–61, https://doi.org/10.1175/1525-7541(2003)004<0043:VORSDI>2.0.CO;2.

Unterstrasser, S., M. Lerch, F. Hoffmann, and I. Sölch, 2017: Collection/aggregation algorithms in Lagrangian cloud microphysical models. *Geosci. Model Dev.*, **10**, 1521–1548, https://doi.org/10.5194/gmd-10-1521-2017.

vanZanten, M. C., and Coauthors, 2011: Controls on precipitation and cloudiness in simulations of trade-wind cumulus as observed during RICO. *J. Adv. Model. Earth Syst.*, **3**, M06001, https://doi.org/10.1029/2011MS000056.

Wang, L. P., and W. W. Grabowski, 2009: The role of air turbulence in warm rain initiation. *Atmos. Sci. Lett.*, **10**, 1–8, https://doi.org/10.1002/asl.210.

Wood, R., 2005: Drizzle in stratiform boundary layer clouds. Part II: Microphysics aspects. *J. Atmos. Sci.*, **62**, 3034–3050, https://doi.org/10.1175/JAS3530.1.